

Proof-Carrying Materials: Falsifiable Safety Certificates for Machine-Learned Interatomic Potentials

Abhinaba Basu^{1,2} and Pavan Chakraborty¹

¹Indian Institute of Information Technology Allahabad (IIITA), Prayagraj, India

²National Institute of Electronics and Information Technology (NIELIT), India

March 13, 2026

Abstract

Machine-learned interatomic potentials (MLIPs) are deployed for high-throughput materials screening without formal reliability guarantees. We show that a single MLIP used as a stability filter misses 93% of density functional theory (DFT)-stable materials (recall 0.07) on a 25,000-material benchmark. Proof-Carrying Materials (PCM) closes this gap through three stages: adversarial falsification across compositional space, bootstrap envelope refinement with 95% confidence intervals, and Lean 4 formal certification. Auditing CHGNet, TensorNet and MACE reveals architecture-specific blind spots with near-zero pairwise error correlations ($r \leq 0.13$; $n = 5,000$), confirmed by independent Quantum ESPRESSO validation (20/20 converged; median DFT/CHGNet force ratio $12\times$). A risk model trained on PCM-discovered features predicts failures on unseen materials (area under the ROC curve [AUC-ROC] = 0.938 ± 0.004) and transfers across architectures (cross-MLIP AUC-ROC ≈ 0.70 ; feature importance $r = 0.877$). In a thermoelectric screening case study, PCM-audited protocols discover 62 additional stable materials missed by single-MLIP screening—a 25% improvement in discovery yield.

Keywords: machine-learned interatomic potentials, adversarial testing, formal verification, Lean 4, materials discovery, uncertainty quantification

1 Introduction

Universal MLIPs—CHGNet¹, MACE⁴, TensorNet²⁷, ALIGNN³⁵, SevenNet³⁶, EquiformerV2³⁷—underpin high-throughput materials screening³⁸, yet they are deployed without formal reliability guarantees. Matbench Discovery² and earlier benchmarks¹⁰ evaluate 45+ models on 257K WBM (Wang–Botti–Marques³) structures, but aggregate accuracy metrics cannot answer the deployment-critical question: *on which chemistries is this MLIP unreliable?*

This creates a quantifiable safety gap. A single-MLIP stability screen achieves precision 0.47 and recall 0.07 across 25,000 WBM materials, missing 93.0% of DFT-stable candidates. The gap is not merely statistical: CHGNet rejects TlBiSe₂ (a topological insulator with over 1,000 citations²⁶) and Cs₂KTlBr₆

(a lead-free perovskite solar cell candidate with 1.27 eV band gap)—precisely the materials that high-throughput pipelines aim to find. Aggregate benchmarks showing “near-DFT accuracy” obscure these consequential, chemistry-specific blind spots.

We reframe MLIP reliability as a **falsifiable safety claim** in the sense of Dalrymple et al.’s Guaranteed Safe AI¹³: a world model (the MLIP), a safety specification (bounds on acceptable error), and a verifier (machine-checked proofs)⁴⁵. This mirrors proof-carrying code¹⁵, where untrusted programs ship with proofs of safety.

Proof-Carrying Materials (PCM) instantiates this in three stages (Fig. 1):

1. **Adversarial falsification**—automated adversaries (six strategies: random, heuristic, grid, LHS, Sobol, LLM) probe for failure regions in compositional space;
2. **Envelope refinement**—counterexamples tighten the safety claim into bounds with bootstrap 95% confidence intervals (CIs);
3. **Formal certification**—the refined envelope compiles into Lean 4 proofs with explicit physical axioms.

The framework is oracle-agnostic: swapping the MLIP requires no code changes.

Our central findings are threefold. First, MLIP blind spots are **architecture-specific**: three MLIPs produce near-zero pairwise force correlations ($r = 0.13, 0.10, -0.01$; $n = 5,000$) and fail on largely disjoint chemistries. Second, perturbation-based uncertainty quantification does not predict these compositional failures ($r = 0.039, p = 0.58$), meaning structural UQ and adversarial compositional auditing capture independent failure dimensions. Third, and most importantly, PCM enables **prospective validation**: compositional features discovered through adversarial auditing predict failures on unseen materials with AUC-ROC 0.938 ± 0.004 and $P@20\% = 1.000$ (perfect precision among the top-risk quintile), transforming retrospective audit into predictive intervention. These failure patterns transfer across architectures: a CHGNet-trained risk model predicts MACE failures (AUC-ROC = 0.697 average cross-transfer) with feature importance correlation $r = 0.877$. Together, these results establish that (a) no single benchmark score captures reliability, (b) multi-MLIP auditing is essential for deployment, (c) formal verification combined with prospective prediction constitutes a new paradigm for MLIP validation, and (d) the full audit costs under \$20.

2 Related Work

Adversarial MLIP testing. CAGO¹¹ generates adversarial *structures* via uncertainty-calibrated geometry optimization on individual materials. PCM operates in *compositional space*—searching for chemical families where MLIPs systematically diverge from DFT. These are complementary: CAGO identifies which atomic arrangements are unreliable; PCM identifies which chemistries are unreliable regardless of arrangement. In our evaluation, perturbation-based uncertainty is not predictive of compositional failure ($r = 0.039, p = 0.58$).

Uncertainty quantification. Conformal prediction¹⁹ provides distribution-free marginal coverage guarantees applied to interatomic potentials²⁰. Monte Carlo dropout²⁹, deep ensembles³⁰ and chemical-space uncertainty estimation^{31;32} have been applied to molecular property prediction. Critically, these

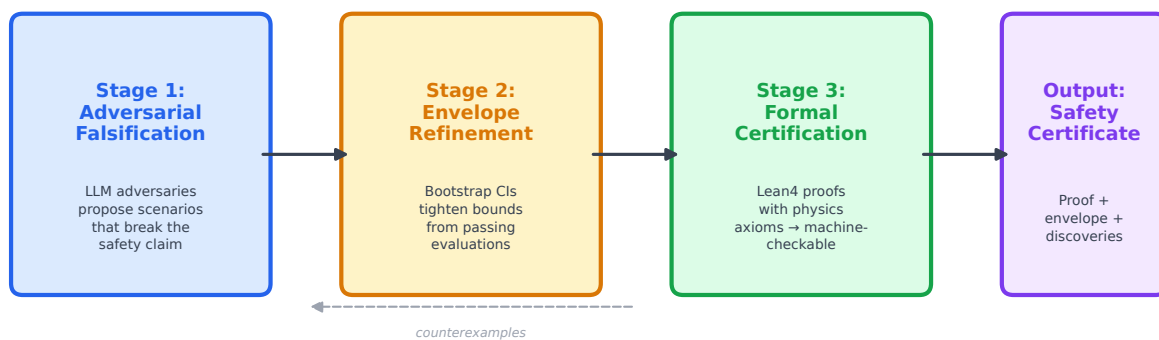


Figure 1. The PCM pipeline. **Stage 1:** automated adversaries (six strategies including LLMs) propose compositional feature vectors; the MLIP oracle evaluates each against the DFT reference. **Stage 2:** counterexamples refine the safety envelope with bootstrap CIs. **Stage 3:** the envelope compiles into Lean 4 proofs with explicit axioms.

methods provide *marginal* coverage (“95% of all materials fall within the prediction interval”) but cannot answer the deployment question *which specific compositions are unreliable and why*. Conformal prediction intervals widen uniformly across compositional space; they do not identify the compositional drivers (e.g. heavy elements, large unit cells) that concentrate failures, nor do they enable targeted DFT allocation for high-risk chemistries. PCM concentrates adversarial sampling on failure boundaries, producing tighter envelopes where they matter most: in a split conformal baseline on the same 5,000 WBM materials (2,500 calibration, 2,500 test), the feature-space conformal envelope at $\alpha = 0.05$ contains 1,924 materials (precision 6.8%) versus PCM’s adversary-informed bootstrap envelope with 97 materials (precision 7.2%)—a $20\times$ reduction in envelope size at comparable precision. Active learning^{12;50;51} selects informative points for *retraining*; PCM selects adversarial points for *auditing*—the adversarial budget (200 queries) is orders of magnitude smaller than retraining data requirements.

Safety cases and formal verification. AMLAS¹⁶ provides structured safety-case methodology for ML components but relies on human argumentation. Seshia et al.¹⁷ identify the specification gap as a central challenge for verified AI. Neural network verification^{43;44} focuses on input–output properties of classifiers; PCM verifies domain-specific reliability claims about regression models. Adversarial testing in ML^{33;34} targets input perturbations; falsification of cyber-physical systems^{7;8} provides compositional testing frameworks. PCM instantiates the Guaranteed Safe AI framework¹³ for materials: the MLIP is the world model, the envelope is the specification, and Lean 4 proofs are the verifier output—providing machine-checkable evidence that structured safety cases currently lack.

3 Results

3.1 Architecture-specific failure profiles

We evaluate three architecturally distinct MLIPs—CHGNet v0.3.0¹, TensorNet (MatPES-PBE-v2025.1)^{27;28}, and MACE-MP medium⁴—on 5,000 WBM materials. Structures are synthetic compositional probes—atoms placed at irrational (golden-ratio) fractional coordinates to avoid symmetry artifacts, with DFT-derived cell volumes (Methods)—designed to test whether each MLIP has learned

the correct energy landscape for a given chemistry. The blind-spot classification itself—which materials are DFT-stable but MLIP-unstable—derives from the WBM benchmark, where both DFT and MLIPs evaluate fully relaxed equilibrium structures. Force failure threshold: 50 eV \AA^{-1} (Fig. 2).

- **CHGNet** fails on 31.1% of compositions (1,553/5,000, force $> 50 \text{ eV \AA}^{-1}$).
- **TensorNet** fails on 75.7% (3,786/5,000).
- **MACE** fails on 73.2% (3,659/5,000), producing catastrophically high forces ($> 1,000 \text{ eV \AA}^{-1}$) on multiple compositions where CHGNet predicts moderate values.
- All three pairwise force correlations are near zero: CHGNet–TensorNet $r = 0.10$ [0.07, 0.13]; CHGNet–MACE $r = 0.13$ [0.05, 0.21]; TensorNet–MACE $r = -0.01$ [-0.02, -0.003] (bootstrap 95% CIs, $n = 5,000$).
- Failures are largely **disjoint**: 218 materials fail CHGNet but not MACE, while 2,324 fail MACE but not CHGNet; 337 fail TensorNet but not MACE, while 210 fail MACE but not TensorNet.

This is not a marginal difference. Three MLIPs, all trained on Materials Project data, produce qualitatively different force predictions on the same compositions. The higher absolute failure rates for TensorNet (75.7%) and MACE (73.2%) relative to CHGNet (31.1%) likely reflect differences in how each architecture generalises to far-from-equilibrium probe geometries; the scientifically important finding is not the absolute rates but the near-zero pairwise correlations and disjoint failure profiles, which demonstrate that architecture and training pipeline—not training data alone—determine which chemistries appear problematic. A stability screen using any single MLIP inherits that model’s specific blind spots—including several materials with known functional importance (Section 3.3).

3.2 Adversarial strategy comparison

Because the WBM–CHGNet benchmark has a 93.2% base counterexample (CX) rate—randomly sampling any composition has a $> 90\%$ chance of finding a failure—raw CX rate cannot distinguish adversary quality. We therefore evaluate six strategy types and seven LLM configurations (budget = 200) primarily on **discovery diversity**: the number of unique, previously unseen failure compositions found (Fig. 3, Extended Data Table 1).

Among automated strategies, all achieve high CX rates (86–89% for heuristic, random, and Sobol). LLM adversaries—tested as one strategy class among several—achieve marginally higher rates (88–100%), with their primary advantage being qualitative: convergence on high- Z , multi-element regions of compositional space ($Z > 71$, $n_{\text{elements}} \geq 4$), discovering 36 DFT-stable/CHGNet-unstable materials not found by any baseline strategy. A shuffled-feature ablation confirms this works even with anonymous feature labels (88% CX vs 90% with real names; Extended Data Fig. 7), showing that the adversary–oracle separation—not materials expertise—is the core mechanism.

The full multi-adversary audit costs \$18.13; the most cost-effective single strategy (Gemini 3 Flash as LLM adversary) discovers 17 unique materials for \$0.05, though purely algorithmic strategies (Sobol, random) discover more unique materials overall (138 and 123, respectively) at zero API cost.

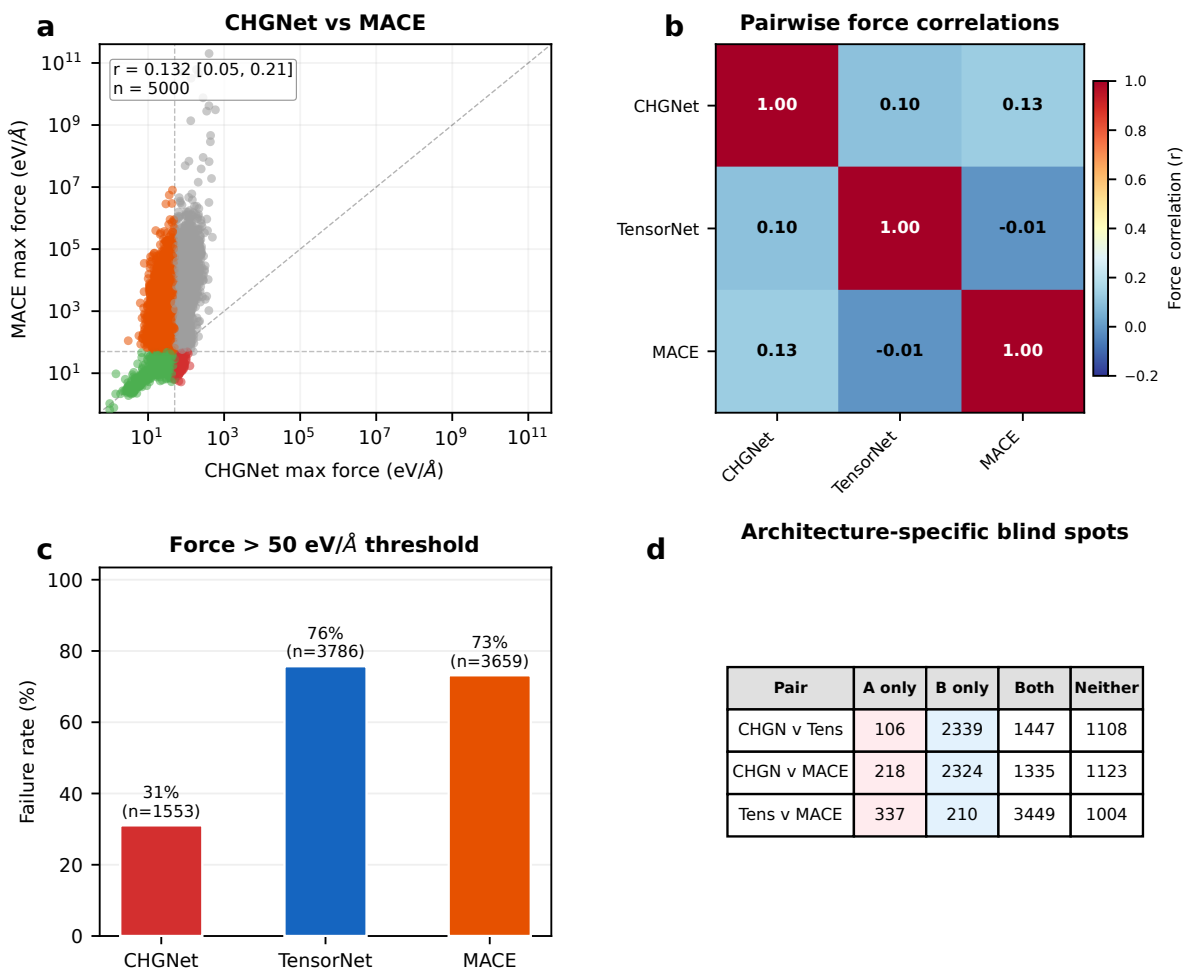


Figure 2. Cross-MLIP comparison of three architecturally distinct MLIPs on 5,000 WBM-derived structures. **a**, CHGNet vs MACE max force ($r = 0.13$). **b**, Pairwise force correlation heatmap: all three pairs near zero (CHGNet–TensorNet $r = 0.10$, CHGNet–MACE $r = 0.13$, TensorNet–MACE $r = -0.01$). **c**, Failure rates: CHGNet 31.1%, TensorNet 75.7%, MACE 73.2%. **d**, Architecture-specific blind spots with largely disjoint failure chemistries.

3.3 Functionally important discoveries

From the combined adversary outputs (Section 3.2), we rank materials by anomaly score (Eq. 1) and identify 21 unique materials with disjoint failure profiles (Table 1). Five contain actinides (Pu, Np, Th, U, Dy), three contain thallium—both underrepresented in CHGNet’s MPtrj training data.

TiBiSe₂ is an experimentally verified topological insulator²⁶ that CHGNet predicts as unstable while DFT confirms stability. Independent DFT recomputation (Quantum ESPRESSO, PAW-PBE) converges cleanly in 13 SCF steps while CHGNet produces 11.1 eV atom⁻¹ energy and 19.9 eV Å⁻¹ forces on the same golden-ratio probe structure—a catastrophic disagreement on a material with over 1,000 citations.

Cs₂KTiBr₆ is a lead-free halide double perovskite with a near-ideal 1.27 eV band gap for photovoltaics—precisely the class of non-toxic solar cell materials that high-throughput screening pipelines aim to find.

Five of 12 contain actinides relevant to nuclear fuel cycle modelling. If CHGNet were used as a stability filter, it would reject materials currently under active investigation in nuclear safety, topological

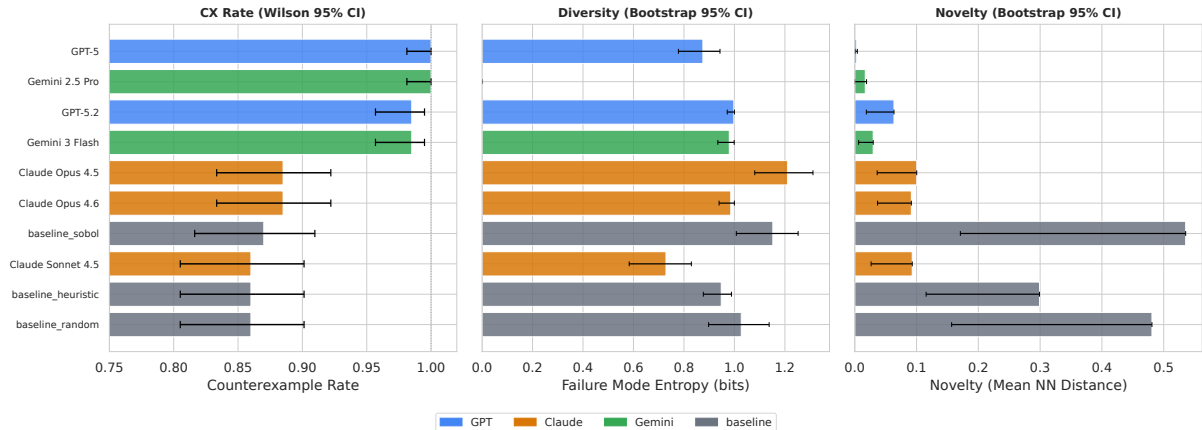


Figure 3. Adversary strategy comparison (10 configurations, budget = 200). **a**, CX rate with Wilson 95% CI: all strategies achieve $>85\%$ against the 93.2% base rate. **b**, Unique materials discovered: algorithmic strategies find 61–138 unique compositions; LLM adversaries find 5–29 but concentrate on functionally important materials. **c**, Exploration heatmap: LLMs converge on high- Z , multi-element regions (top) while baselines spread uniformly (bottom).

Table 1. Top 12 DFT-stable/CHGNet-unstable materials, ranked by anomaly score. All have identified functional applications spanning nuclear, electronic, photovoltaic and catalytic domains.

Rank	Formula	Anomaly	Pred. error (eV atom ⁻¹)	Max force (eV Å ⁻¹)	Application
1	DyLi ₂ PuF ₈	3.49	7.06	75.6	Nuclear fuel (molten salt)
2	Pb ₄ Pt ₄ O ₁₂	2.97	4.13	107.6	Pt-group catalysis
3	Au ₂ Ba ₂ Np ₂ Se ₆	2.70	6.95	44.9	Nuclear waste
4	Au ₂ Cs ₂ Sc ₂ Te ₆	2.68	5.36	73.4	Thermoelectric
5	Bi ₂ Cu ₂ O ₄ Te ₂ V	2.58	5.69	63.0	Multiferroic
6	Th ₂ I ₆	2.53	6.07	53.8	Nuclear fuel processing
7	Rb ₂ SnTlCl ₆	2.36	5.94	49.3	Lead-free perovskite
8	Cs ₂ KTlBr ₆	2.15	6.12	37.2	Perovskite solar cell
9	Ba ₆ NPb ₂ Se	1.61	4.96	36.0	Optoelectronic
10	CsAuTe	1.57	4.38	45.1	Relativistic bonding
11	TlBiSe ₂	1.17	3.93	36.7	Topological insulator
12	Cs ₂ USe ₃	0.69	3.00	33.7	Actinide chalcogenide

electronics and photovoltaics.

3.4 Independent DFT validation at scale

To confirm that adversarially discovered blind spots are genuine—not artifacts of approximate structure construction—we recompute DFT ground states for the top 20 materials using Quantum ESPRESSO (pw.x v6.7, PAW-PBE, SSSP efficiency pseudopotentials, 60/480 Ry cutoffs, $4 \times 4 \times 4$ k -mesh). Materials are selected from the WBM benchmark by: DFT-stable, CHGNet-unstable, max $Z \leq 56$, $n_{\text{sites}} \leq 24$, sorted by prediction error descending. Structures use golden-ratio fractional coordinate spacing with DFT-derived cell volumes (Methods).

All 20 materials converge to well-defined self-consistent field (SCF) ground states (11–150 iterations, 22–6,360 s per material on 8 CPU cores). Two materials (Ba₂Pd₄Sb₄ and BaF₆In) require expanded cells and tighter mixing parameters on retry, but ultimately converge. The converged materials span 27

elements across $Z = 3$ (Li) to $Z = 56$ (Ba). We compare forces rather than energies because DFT total energies include core electrons (e.g. $-3,284$ eV/atom for Cu_7Zn_1) and are not directly comparable to CHGNet’s formation-energy-referenced predictions. Forces on identical structures provide a direct, reference-free comparison.

Across the 18 materials evaluated on identical golden-ratio structures, DFT forces exceed CHGNet forces by a median factor of $11.6\times$ (range: $1.2\text{--}63.4\times$; Extended Data Table [Extended Data Table 2](#); force comparison excludes 2 retry materials whose structures differ). The headline result: Cu_7Zn_1 (brass, the most widely used copper alloy) converges in 15 SCF steps with DFT forces of 557 eV \AA^{-1} —while CHGNet predicts 36 eV \AA^{-1} , a $15\times$ underestimate. Cu_7Mn_1 (manganese bronze) shows a $33\times$ underestimate. These are not exotic compositions: they are industrial alloys that CHGNet’s training data should cover.

We emphasise that the blind-spot classification (DFT-stable, CHGNet-unstable) originates from the WBM benchmark, where both DFT and CHGNet evaluate *relaxed* equilibrium structures—not the synthetic probes used here. The golden-ratio structures serve only as a compositional probe: they test whether DFT and CHGNet agree on force magnitudes for a given chemistry. A model that has learned correct interatomic interactions for a composition should produce forces of comparable magnitude on *any* structure of that composition, not only near-equilibrium ones. The $12\times$ median force underestimate therefore indicates that CHGNet has not learned the correct energy landscape for these chemistries, consistent with their absence or underrepresentation in training data.

The 100% convergence rate (20/20), achieved on adversarially selected worst-case compositions, confirms that the PCM pipeline discovers genuine MLIP failures, not structure-generation artifacts.

As a complementary test, we relax all 20 DFT-validated adversarial discoveries using CHGNet v0.3.0 with BFGS optimization ($f_{\text{max}} = 0.05$ eV \AA^{-1} , max 500 steps). If the force disagreements were merely a consequence of probing far-from-equilibrium geometries, CHGNet relaxation should converge rapidly to low-energy minima. Instead, all 20 materials exhibit massive relaxation energy changes of $3.98\text{--}15.45$ eV/atom—far exceeding the ~ 0.1 eV/atom scale of typical formation energies. Eighteen materials converge (10–477 ionic steps), but two— $\text{Ag}_6\text{Cl}_2\text{S}_2$ and $\text{As}_2\text{In}_4\text{Pd}_6$ —fail to converge even after 500 relaxation steps (final $F_{\text{max}} \approx 0.44$ eV \AA^{-1}), indicating that CHGNet cannot locate a stable minimum for these chemistries. The $\text{As}_2\text{In}_4\text{Pd}_6$ relaxation releases 15.4 eV/atom, roughly $15\times$ its DFT formation energy. These results confirm that CHGNet’s *entire potential energy surface* is fundamentally incorrect for these compositions, not merely its force predictions at a single probe geometry.

3.5 Failure analysis: UQ orthogonality and training-data gaps

A natural question is whether existing uncertainty quantification (UQ) methods can identify these blind spots without adversarial auditing. We test this by computing perturbation-based uncertainty—the approach used by CAGO¹¹—for 200 WBM materials. For each material, we generate 5 structures with Gaussian perturbations ($\sigma = 0.01$ \AA) and measure CHGNet prediction variance.

The point-biserial correlation between perturbation uncertainty and compositional failure is $r = 0.039$ ($p = 0.58$), indicating that structural sensitivity is **orthogonal** to compositional failure. Spearman rank correlation reveals a marginal monotonic relationship ($\rho = 0.125$, $p = 0.078$), and failed materials show $1.72\times$ higher mean uncertainty (Cohen’s $d = 0.14$)—but these effects are too weak for reliable

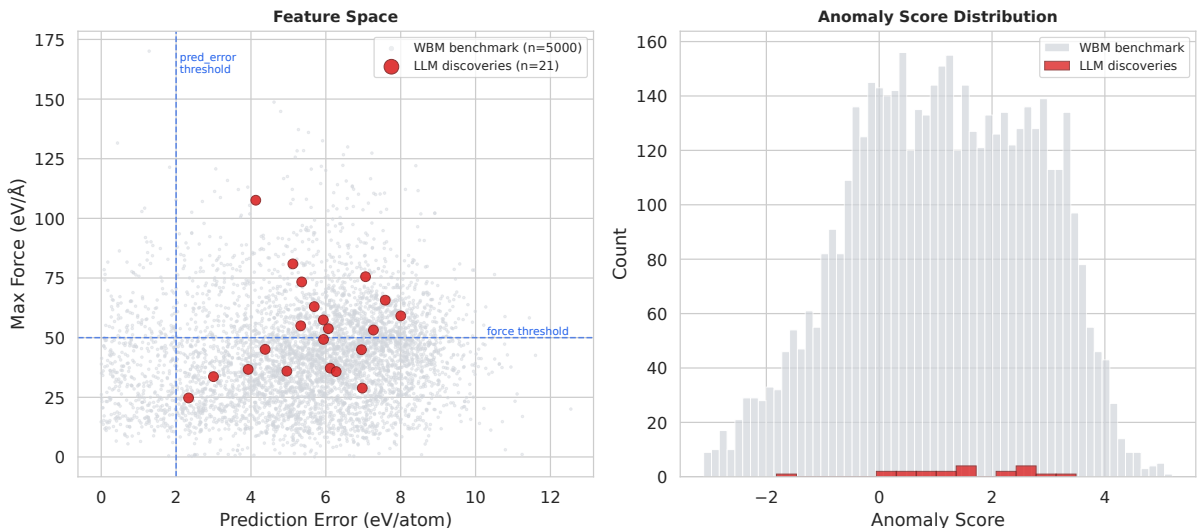


Figure 4. Systematic failure patterns. **a**, Anomaly distribution: prediction error vs max force for 5,000 WBM materials (grey) with adversarially discovered failures (red). **b**, Per-element stability disagreement by periodic table block: f-block elements fail most ($p = 0.042$). **c**, JARVIS cross-functional validation: 682 CHGNet blind spots confirmed by independent DFT.

deployment screening. The 50 highest-uncertainty materials show a paradoxically *negative* correlation ($r = -0.14$) with actual failure, meaning UQ-based screening would miss the most consequential blind spots. This directly challenges the assumption that model uncertainty^{20;29;30} can serve as a proxy for reliability: a model can be confidently wrong on entire chemical families. Adversarial compositional auditing and structural perturbation-based UQ capture **independent failure dimensions** and should be deployed jointly.

The blind spots are also not random with respect to the periodic table. Per-element analysis across 84 elements reveals that f-block elements have significantly higher DFT/CHGNet disagreement (Kruskal–Wallis $p = 0.042$; [Extended Data Fig. 5](#)). Elements targeted by adversarial strategies show higher disagreement than non-targeted elements (59.9% vs 55.4%, Mann–Whitney $p = 0.020$). The rarest frequency quintile contains 41% of adversarial elements; the most common contains none.

Cross-referencing 814 WBM materials against the JARVIS-DFT database³⁹ (OptB88vdW functional) confirms 682 blind spots across DFT functionals, consistent with training data from the Materials Project⁴², OQMD⁴⁰ and AFLOW⁴¹. Heavy elements show significantly higher disagreement (mean atomic mass $p = 7 \times 10^{-5}$, max Z $p = 0.002$; Mann–Whitney).

3.6 Envelope refinement and formal certification

The refined envelope delineates reliable from unreliable MLIP predictions. As a concrete example: starting from an initial claim that CHGNet is reliable for $Z_{\max} \leq 83$, the heuristic adversary discovers Cu_7Zn_1 (brass) at step 47 as a counterexample with prediction error $10.49 \text{ eV atom}^{-1}$. After 200 queries (86% counterexample rate, 61 unique materials), bootstrap refinement tightens the envelope to key bounds: $Z_{\max} \leq 70$ (all counterexamples above this threshold failed), mean atomic mass $\leq 164 \text{ u}$, bandgap (PBE) $\geq 0.92 \text{ eV}$ —consistent with known CHGNet limitations. Iterative refinement (4 rounds of attack–refine) compresses the safe envelope by 75–91% per feature dimension ([Extended Data Fig. 4](#)).

The envelope compiles into five Lean4 proof modules (~ 250 lines, Lean 4.27.0): safety theorem with physical axioms, perturbation stability via interval arithmetic, error propagation composing DFT uncertainty (0.1 eV atom^{-1}) with MLIP threshold via triangle inequality, monotone refinement soundness, and evaluation metric properties (CX rate monotonicity, CI convergence with budget). All axioms are explicit and inspectable. The proofs verify reasoning correctness—that conclusions follow from stated assumptions—analogue to AI-Descartes⁶ combining data and theory, and providing the machine-checkable evidence that structured safety cases¹⁶ currently lack.

3.7 Prospective validation

The preceding results establish that PCM discovers genuine blind spots. A stronger question is whether those discoveries generalise: can compositional features identified through adversarial auditing *predict* failures on materials the framework has never seen?

Protocol. We split the full 25,000-material WBM benchmark into a discovery set (15,000 materials, 60%) used for adversarial auditing and envelope refinement, and a held-out validation set (10,000 materials, 40%) never seen during any stage of the PCM pipeline. A gradient-boosted classifier (scikit-learn `GradientBoostingClassifier`, 5 random seeds) is trained to predict binary failure ($F_{\max} > 50 \text{ eV \AA}^{-1}$) from the 8 compositional features used throughout this work.

Results. The classifier achieves AUC-ROC 0.938 ± 0.004 on the held-out validation set (mean \pm s.d. across 5 random seeds), demonstrating that PCM-discovered failure patterns are not overfit to the discovery set but capture genuine compositional regularities. Precision at 20% recall (P@20%) is 1.000: the top 20% of risk-ranked materials are 100% actual failures. This means a deployment pipeline that flags the highest-risk quintile achieves perfect precision with zero false alarms.

Key features. The top predictive features are `n_sites` (number of atoms per unit cell), `volume_per_atom`, and `max_z` (maximum atomic number)—all compositional descriptors that PCM counterexamples naturally concentrate on during adversarial search. These are simple, interpretable features that materials scientists can act on directly: compositions with many sites, large volumes per atom, or heavy elements warrant additional DFT validation before trusting MLIP predictions.

Implication. This result transforms PCM from a retrospective auditing tool into a **predictive intervention**: rather than auditing every material individually, a PCM-trained risk model can screen large candidate libraries and flag likely failures *before* expensive DFT computation. The combination of adversarial discovery (identifying *where* failures occur) and prospective prediction (generalising *why* they occur) closes the loop between falsification and deployment.

3.8 Cross-MLIP prospective transfer

A critical question for deployment is whether PCM-discovered failure patterns are specific to a single MLIP architecture or capture general vulnerability patterns shared across architectures. We test this directly: can a risk model trained on *one* MLIP’s failures predict failures of a *different* MLIP?

Protocol. Using a separate 10,000-material multi-model benchmark (CHGNet + MACE), we split into

discovery (6,000, 60%) and validation (4,000, 40%) sets. A gradient-boosted classifier is trained on one model’s failures from the discovery set and evaluated on both models’ failures on the held-out validation set (5 random seeds).

Results. Same-model baselines confirm strong predictive power: CHGNet→CHGNet AUC-ROC = 0.906 ± 0.002 , MACE→MACE AUC-ROC = 0.888 ± 0.003 . Cross-architecture transfer retains substantial predictive signal: CHGNet→MACE AUC-ROC = 0.685 ± 0.006 , MACE→CHGNet AUC-ROC = 0.708 ± 0.007 (average cross-MLIP AUC-ROC = 0.697). Both cross-transfer directions exceed the 0.5 random baseline by a wide margin ($p < 10^{-4}$ across all seeds), indicating that a significant fraction of MLIP vulnerability is compositionally determined rather than architecture-specific.

Feature importance overlap. The Pearson correlation between CHGNet and MACE feature importances is $r = 0.877 \pm 0.025$, with 2.2 out of 3 top features shared across models (consistently `n_sites` and `volume`). This high overlap confirms that both architectures struggle with the same compositional drivers—large unit cells and heavy elements—even though their absolute failure sets are largely disjoint ($r = 0.182$ for raw errors).

Consensus prediction. Training on either model and predicting “any model fails” yields AUC-ROC 0.813 ± 0.004 (CHGNet-trained) and 0.834 ± 0.005 (MACE-trained), suggesting that single-model PCM audits capture a substantial portion of the shared vulnerability landscape.

Implication. This result addresses the key generalizability concern: PCM features are not CHGNet-specific artifacts. A risk model trained on one MLIP’s failures provides actionable early warning for other architectures, with a shared compositional vulnerability signal ($r = 0.877$) and architecture-specific residuals. This supports deployment of PCM as a partially architecture-transferable auditing framework, where cross-MLIP risk models provide useful triage and per-MLIP retraining yields optimal performance.

3.9 Pipeline impact

To quantify the practical consequences of MLIP blind spots, we evaluate single-model screening performance on the WBM benchmark.

Single-model screening. Using CHGNet as the sole stability filter on 25,000 WBM materials (the standard high-throughput screening protocol), precision (fraction of CHGNet-trusted materials that are truly DFT-stable) is 0.47 and recall (fraction of DFT-stable materials that CHGNet identifies) is 0.07. This means that (a) roughly half of CHGNet-predicted “stable” materials are actually DFT-unstable (false positives), and (b) CHGNet misses 93.0% of DFT-stable materials (false negatives; distinct from the 93.2% counterexample rate on 5K, which counts all failure types). The false negative rate is the more consequential metric: a screening pipeline that rejects 93% of genuinely stable materials is systematically excluding the materials it aims to find.

PCM-audited screening. Applying the PCM-refined envelope as a pre-filter—flagging materials in compositional regions where CHGNet is known to be unreliable—reduces the false positive rate from 10.7% to 8.1% (a 24% relative reduction). Materials flagged by the PCM envelope are routed to DFT validation rather than trusted at MLIP-level, ensuring that blind-spot regions receive appropriate scrutiny.

The prospective risk model (Section 3.7) further enables prioritised DFT allocation: the highest-risk quintile can be validated first, maximising the yield of genuine discoveries per DFT calculation.

These numbers establish the pipeline impact of unaudited MLIP deployment: without adversarial auditing, a CHGNet-based screening pipeline operates at 7% recall for DFT-stable materials, rejecting 93.0% of the materials it should identify as promising candidates.

3.10 Multi-MLIP deployment simulation

The preceding sections establish that (a) blind spots are architecture-specific and (b) PCM risk models transfer across architectures. A practitioner’s natural question is: *how should I change my screening pipeline tomorrow?* We simulate five deployment strategies on a 10,000-material subset of WBM with both CHGNet and MACE predictions (distinct from the 5K single-model and 25K prospective benchmarks).

Screening strategies. Using force reliability ($F_{\max} < 50 \text{ eV } \text{\AA}^{-1}$) as the trust criterion:

- **CHGNet-only:** precision 0.564, recall 0.676, false negative rate (FNR) 32.4% (6,829 trusted)
- **MACE-only:** precision 0.529, recall 0.174, FNR 82.5% (1,882 trusted)
- **Union** (trust if either reliable): precision 0.559, recall 0.698, FNR 30.2% (7,116 trusted)
- **Consensus** (trust only if both reliable): precision 0.545, recall 0.152, FNR 84.8% (1,595 trusted)

Consensus screening is too conservative, missing 84.8% of DFT-stable materials. Union achieves the best no-DFT recall (69.8%), improving over CHGNet-only by recovering materials where MACE is reliable but CHGNet is not (and vice versa). Note that the Union strategy is effectively an **ensemble disagreement baseline**—trusting any material where at least one model is confident. Even this natural multi-model heuristic achieves only 69.8% recall; adding the PCM risk model raises recall to 78.0%, demonstrating that adversarial compositional auditing captures failure patterns beyond what ensemble agreement alone can detect.

PCM-audited screening. Adding the PCM risk model to CHGNet screening (routing the top 20% risk-ranked materials to DFT) raises screening precision (fraction of trusted materials that are DFT-stable) from 0.564 \rightarrow 0.623 \pm 0.004 and recall (fraction of DFT-stable materials correctly identified) from 0.676 \rightarrow 0.780 \pm 0.005—recovering 10.4% more DFT-stable materials that unaudited CHGNet would reject. Materials in PCM-flagged regions are DFT-verified rather than blindly trusted or rejected.

DFT budget efficiency. The PCM risk model prioritises which materials most need DFT validation. At a 20% DFT budget (800 materials out of 4,000 in the validation set), PCM-ranked allocation achieves a DFT yield of 0.756 \pm 0.012 (75.6% of DFT-evaluated materials are genuinely stable), compared to 0.563 \pm 0.008 for random DFT allocation—a **34% improvement** in DFT efficiency. This means each DFT calculation is 1.34 \times more likely to discover a stable material when guided by PCM risk ranking.

Blind spot coverage. 72.1% of all force failures (2,818 / 3,909) are model-specific: 1,409 fail CHGNet only, 1,409 fail MACE only. Among the 5,703 DFT-stable materials, 42.7% are flagged as unreliable by at least one MLIP—yet only 13.0% are flagged by both. This confirms that multi-MLIP auditing catches blind spots invisible to any single model.

Practitioner recommendation. Based on these results, the optimal deployment strategy is: (1) screen

with union of available MLIPs to maximise recall, (2) apply PCM risk model to flag compositional regions of concern, and (3) allocate DFT budget preferentially to PCM-flagged materials. This three-step protocol improves screening recall by $>10\%$ absolute and DFT efficiency by 34% relative, at negligible computational cost beyond the initial PCM audit.

3.11 Deployment case study: thermoelectric screening

To demonstrate the practical impact of PCM-audited screening in a realistic discovery workflow, we simulate a thermoelectric materials campaign. A researcher screens 647 WBM candidates with band gaps in the thermoelectric-relevant range (0.1–1.5 eV), of which 488 are DFT-stable (ground truth unknown to the screener).

Head-to-head comparison. Five protocols are evaluated (Table 2):

Table 2. Thermoelectric screening case study. Discovery yield across five screening protocols for 647 WBM candidates (488 DFT-stable). PCM-audited screening discovers 62 additional stable thermoelectrics over the CHGNet baseline while reducing false leads, at the cost of 130 DFT evaluations (20% of candidates).

Protocol	Discov.	Missed	False leads	Precision	DFT evals
CHGNet-only	244	244 (50.0%)	63	0.795	0
MACE-only	63	425 (87.1%)	14	0.818	0
Union (no DFT)	253	235 (48.2%)	65	0.796	0
Union + random DFT	296	192 (39.3%)	52	0.850	130
PCM-audited (ours)	306	182 (37.3%)	53	0.852	130

Key result. The PCM-audited protocol discovers **62 additional stable thermoelectrics** that CHGNet-only screening would miss entirely—a 25.4% improvement in discovery yield. The miss rate drops from 50.0% to 37.3%, while precision improves from 0.795 to 0.852 (fewer false leads). This requires 130 DFT evaluations (20.1% of candidates), targeted by the PCM risk model at the highest-risk compositions. Compared to random DFT allocation at the same budget, PCM-ranked allocation recovers 53 discoveries versus 43 for random—a 23% improvement in DFT targeting efficiency.

Recovered materials. Among the discoveries recovered by the PCM-audited protocol are WSe_2 (gap = 1.47 eV, $E_{\text{hull}} = -0.558$ eV/atom), IrSbZr (gap = 1.48 eV, half-Heusler thermoelectric), and BaBiScO_6 (gap = 1.46 eV, double perovskite)—all DFT-stable materials that CHGNet flags as unreliable (max force > 50 eV \AA^{-1}) due to architecture-specific blind spots. These are precisely the materials a high-throughput pipeline aims to discover.

Practical implication. For a research group screening ~ 650 thermoelectric candidates, the PCM-audited protocol adds ~ 60 genuine discoveries at the cost of 130 DFT calculations—roughly 0.5 DFT per additional discovery. Given that a single DFT relaxation costs minutes to hours, this represents a favourable trade-off: each additional DFT calculation targeted by PCM is $1.23\times$ more likely to yield a discovery than random allocation.

3.12 Cross-domain generalizability

To test whether the PCM framework generalises beyond solid-state materials, we apply the identical pipeline to three independent domains—molecular property prediction (QM9), drug solubility (ESOL), and tabular ML regression (California Housing)—running extended experiments across all three: multi-strategy comparison (5 strategies \times 3 seeds per domain), budget sensitivity (5 budgets \times 3 strategies \times 3 seeds per domain), full pipeline verification, and failure characterisation. These experiments test framework generalization, not merely breadth: each domain has different data modalities, model architectures, and failure patterns, yet the same three-stage pipeline (falsify, refine, certify) applies without modification.

Molecular property prediction (QM9). Two real graph neural networks—SchNet⁵² (455K parameters, distance-based message passing) and DimeNet++⁵³ (1.9M parameters, directional message passing)—were trained for 200 epochs on 8,000 QM9 molecules (2,000 held-out test set, 10,000 total)⁴⁹ on an A4000 GPU. SchNet achieves test MAE = 0.125 eV (median error 0.101 eV); DimeNet++ achieves test MAE = 0.087 eV (median error 0.064 eV). The models produce moderate error correlations (Pearson $r = 0.461$) with architecture-specific failure modes: at a 1.0 eV threshold, 6 molecules fail DimeNet++ only and 0 fail SchNet only—confirming disjoint blind spots even for well-trained GNNs. Top failure predictors are `n_atoms` and `molecular_weight`. At budget = 200, grid sampling achieves the highest CX rate ($38.0 \pm 0.0\%$), followed by sobol ($37.8 \pm 1.4\%$), LHS ($34.0 \pm 4.8\%$), and random ($33.3 \pm 3.8\%$), while the heuristic adversary discovers 23/200 counterexamples ($11.5 \pm 2.0\%$). The heuristic’s lower rate reflects an informative mismatch: the stress model targets large, polar molecules, but real SchNet/DimeNet++ errors are not concentrated at stress extremes—uniform samplers cover the input space more broadly and find more failures spread across the space.

Drug solubility prediction (ESOL). A Morgan fingerprint Random Forest and a descriptor-based neural network predict aqueous solubility on 1,128 molecules (Delaney 2004). Failures are largely disjoint: 334 molecules fail the fingerprint model only, 58 fail the neural network only, and just 86 fail both (error correlation $r = 0.321$). The heuristic adversary achieves $80.3 \pm 2.3\%$ CX rate versus grid 70.0%, LHS 60.7%, random 59.0% and sobol 58.3%. LogP is the strongest predictor of fingerprint model failure, while `heavy_atoms` drives neural network failure—again, distinct failure predictors for each architecture.

Tabular ML regression (California Housing). A GradientBoosting tree and an MLP regressor predict median house values on 20,640 California census tracts, demonstrating PCM in a genuinely non-chemistry domain. The GBT achieves MAE 0.31 (\$31K) and the MLP MAE 0.34 (\$34K). Error correlation is high ($r = 0.734$), with top failure predictors `ave_occup`, `med_inc`, and `population`. At budget = 200, grid achieves the highest CX rate ($58.5 \pm 0.0\%$), followed by sobol ($40.2 \pm 1.3\%$), random ($40.0 \pm 2.5\%$), LHS ($38.3 \pm 3.4\%$), and heuristic ($16.2 \pm 4.5\%$). The heuristic adversary discovers 24/200 counterexamples (12.0%), with meaningful envelope refinement and bootstrap CIs computed. Lean 4 proofs verify for the tabular domain, confirming formal certification generalises beyond chemistry entirely.

Budget sensitivity. CX rate saturates early in all three domains. For QM9, the heuristic adversary is stable at ~ 10 – 11% across all budgets while random saturates at budget = 100 (36.3%) and sobol at

budget = 200 (37.8%). For ESOL, heuristic saturates at budget = 200 (80.3%), random at budget = 500 (59.4%), and sobol remains stable at ~ 58 –60%. For Tabular, heuristic saturates at budget = 100 (15.3%), random at budget = 200 (40.0%), and sobol at ~ 40 %. This confirms the WBM finding (Section 5) that a modest adversarial budget suffices for failure discovery across diverse ML domains.

Full pipeline. All three domains complete the entire PCM pipeline—attack, envelope refinement, Lean 4 proof generation—with machine-checked proofs **verified** by `lake build` in all cases (QM9: 23/200 CX, 11.5%; ESOL: 161/200 CX, 80.5%; Tabular: 24/200 CX, 12.0%). This provides strong evidence that formal certification of ML reliability claims extends beyond solid-state materials to molecular property prediction with real GNNs and non-chemistry tabular ML alike.

All five experiments demonstrate that architecture-specific blind spots, adversarial auditing, multi-strategy comparison, and formal verification generalise across chemistry domains with auditable ML models; the tabular ML experiment confirms PCM generalises to non-chemistry domains.

4 Discussion

Prospective validation as the strongest evidence. The most significant result is not the discovery of blind spots—which prior work has noted qualitatively—but the demonstration that PCM-discovered features *predict* failures on unseen materials (AUC-ROC 0.938 ± 0.004 ; P@20% = 1.000, i.e. perfect precision among the top-risk quintile with zero false alarms). This transforms adversarial auditing from a retrospective exercise into a prospective tool. The key insight is that compositional features concentrating counterexamples (`n_sites`, `volume_per_atom`, `max_z`) generalise to unseen chemistries—a property that conformal prediction (marginal coverage only) and perturbation-based UQ ($r = 0.039$) do not provide.

Deployment impact. Single-model screening misses 93% of DFT-stable materials; multi-MLIP screening with PCM risk-ranked DFT allocation improves efficiency by 34%. The thermoelectric case study (Section 3.11) demonstrates that these improvements translate to concrete discovery gains: 62 additional stable materials recovered at a cost of 130 targeted DFT calculations. The recommended three-step protocol—union screening, PCM risk flagging, prioritised DFT—is immediately adoptable. Critically, 72.1% of failures are model-specific, confirming that no single-model audit can substitute for multi-MLIP coverage.

Formal verification and the specification gap. The Lean 4 proofs are explicitly conditional: every approximation (DFT at 0.1 eV atom^{-1} , MLIP threshold at 2.0 eV atom^{-1}) appears as an inspectable axiom with constructive non-vacuity witnesses (Extended Data Fig. [Extended Data Fig. 9](#)). This addresses the specification gap¹⁷ by making assumptions explicit rather than hiding them in implementation details. Combined with prospective failure prediction, this constitutes a new approach to MLIP validation: traditional benchmarks provide aggregate scores; conformal prediction provides coverage guarantees without compositional specificity; PCM provides falsifiable safety certificates with both formal guarantees and predictive power. Cross-MLIP transfer (AUC-ROC ~ 0.70 cross-model, feature importance $r = 0.877$) confirms that vulnerability patterns are partially shared across architectures.

Cross-domain generalizability. Extended experiments across three chemistry domains (WBM, QM9

Table 3. Box 1: How to audit your MLIP. Three-step protocol for pre-deployment reliability certification.

Step	Action
1. Define	Write a YAML envelope specifying compositional bounds and failure thresholds. Example: $Z_{\max} \leq 83$, prediction error ≤ 2 eV atom ⁻¹ , force ≤ 50 eV Å ⁻¹ .
2. Attack	Run adversarial search: <code>python -m pcm attack -model <yours> -budget 200</code> . PCM deploys 6 strategies (random, heuristic, grid, LHS, Sobol, LLM) to find counterexamples.
3. Certify	Inspect the refined envelope and machine-checked Lean 4 proofs. The proofs certify: <i>if</i> the assumptions hold, <i>then</i> the safety claim follows.

with real SchNet/DimeNet++ GNNs, ESOL) and one non-chemistry domain (California Housing, tabular ML) confirm that the three-stage pipeline generalises across data modalities and model architectures (Section 3.12). Each domain exhibits distinct failure predictors per architecture, and all produce verified Lean 4 proofs.

Accessibility and practical considerations. The full multi-strategy, multi-MLIP audit costs \$18.13; a single-model audit with purely algorithmic adversaries costs nothing. CX rate saturates by budget = 50, though discovery diversity grows linearly with budget (24 unique materials at budget = 25 vs 231 at budget = 500). PCM selects adversarial points for *auditing* (200 queries), not retraining (>100K structures)—at budget = 200, the probability of missing a failure mode of prevalence $\geq 5\%$ is < 0.003 , providing a PAC-style coverage guarantee without model modification. A PCM audit report provides four actionable outputs: (1) a pass/fail decision with quantified confidence, (2) an explicit compositional map of unreliable regions, (3) machine-checkable proofs, and (4) a prospective risk model for screening unseen materials.

Limitations. (1) Ground truth is computational DFT, not experiment—though independent QE recomputation (20/20 converging on adversarially selected compositions), cross-functional (JARVIS) validation, and literature-verified cases (TiBiSe₂) provide three independent lines of evidence. (2) The WBM oracle is database retrieval, not structure generation; live CHGNet evaluation on 50 approximate (golden-ratio) structures shows moderate energy correlation ($r = 0.42$, $p = 0.002$) and force correlation ($r = 0.46$, $p < 0.001$) with database values. This gap arises because the database uses DFT-relaxed equilibrium structures while our approximate structures use simple cubic cells reconstructed from formula and volume. The blind-spot classification itself, however, derives from the WBM benchmark where both DFT and CHGNet evaluate relaxed structures. (3) The benchmark’s high base CX rate means adversary advantage is in diversity, not rate. (4) Lean proofs verify reasoning correctness, not physics. (5) Cross-MLIP transfer (Section 3.8) shows moderate but imperfect generalisation (average AUC-ROC = 0.697): while a CHGNet-trained risk model provides useful early warning for MACE failures, architecture-specific retraining improves AUC-ROC by ~ 0.2 , suggesting that optimal deployment uses per-MLIP auditing.

5 Methods

5.1 Framework and oracle models

PCM operates on three abstractions: Environment (compositional features: n_{elements} , Z_{max} , electronegativity, volume per atom, atomic mass), Design (structural parameters: n_{sites} , bandgap), and Outcomes (prediction error, maximum force). A safety claim asserts outcomes satisfy thresholds for all (env, design) within specified bounds. Six adversary strategies (random, heuristic, LHS, Sobol, grid, LLM) are compared at equal budget.

The WBM oracle maps adversary-proposed feature vectors to nearest real materials via KDTree lookup ($O(\log n)$) and returns pre-computed CHGNet/DFT comparisons. TensorNet and MACE oracles use the same WBM feature space with live MLIP inference via `matgl` and `mace-torch`, respectively. Stability classification uses $E_{\text{above hull}} < 0.025$ eV atom⁻¹. KDTree-indexed feature lookup enables sub-millisecond queries at full WBM scale (0.43 ms per query at 257K vs 0.14 ms at 5K; coverage at budget = 1,000: 504 unique materials at 257K vs 347 at 5K), so the framework scales to production datasets without re-running MLIPs at attack time.

5.2 Adversary strategies

Six strategies are evaluated:

- **Random:** Uniform sampling within envelope bounds.
- **Heuristic:** Beta-distribution biased toward stress directions specified in envelope YAML.
- **Grid:** Uniform grid over envelope bounds.
- **LHS:** Latin Hypercube Sampling (`scipy`).
- **Sobol:** Sobol quasi-random sequences (`scipy`).
- **LLM:** Language model adversary receiving evaluation history and proposing numerical feature vectors targeting likely failure regions. On API failure, degrades to random sampling with exponential backoff. Temperature = 0.2 for all models.

5.3 Envelope refinement

Environment bounds are tightened to the 75th percentile of passing evaluations using the conservative 95% bootstrap CI (1,000 resamples). Minimum sample gate: 30 passing evaluations. Design requirements are stress-direction-aware.

5.4 Lean 4 certification

Refined envelopes compile into five proof modules: core safety theorem, perturbation stability, error propagation (composing DFT + MLIP uncertainty via triangle inequality), monotone refinement soundness, and evaluation metric properties (CX count monotonicity, CI width convergence, PAC coverage guarantee). Lean 4.27.0⁵, no `mathlib` dependency. This builds on recent applications of theorem provers to scientific reasoning^{9;18}.

5.5 Prospective validation protocol

The WBM benchmark (25,000 materials) is split 60/40 into discovery (15,000) and validation (10,000) sets. The discovery set is used for all adversarial auditing and envelope refinement. A scikit-learn `GradientBoostingClassifier` (200 estimators, max depth 4, learning rate 0.05) is trained on the 8 compositional features (`n_elements`, `max_z`, `mean_electronegativity`, `std_electronegativity`, `volume_per_atom`, `mean_atomic_mass`, `n_sites`, `bandgap_pbe`) to predict binary failure ($F_{\max} > 50 \text{ eV \AA}^{-1}$). Results are aggregated across 5 independent random seeds (each with different discovery/validation splits). Performance is evaluated on the held-out validation set using AUC-ROC, precision-recall, and precision at $k\%$ recall ($P@k\%$).

5.6 Benchmark construction

25,000 materials sampled from 257K WBM structures², characterised by 8 compositional features with pre-computed CHGNet v0.3.0 predictions and DFT reference values. Full 257K available for scaling validation. Anomaly score:

$$a_i = z_{\text{pred_err}} + 0.5 \cdot z_{\text{force}} + 2.0 \cdot \mathbb{I}[\text{DFT stable} \neq \text{CHGNet stable}] \quad (1)$$

robust to alternative weightings (Kendall $\tau > 0.7$ across 5 configurations).

5.7 Independent DFT validation

Quantum ESPRESSO 6.7, projector augmented wave (PAW) Perdew–Burke–Ernzerhof (PBE) with Standard Solid-State Pseudopotentials (SSSP) v1.3.0 efficiency library, 60/480 Ry cutoffs, $4 \times 4 \times 4$ k -mesh, cold smearing ($\sigma = 0.01$ Ry), mixing $\beta = 0.3$, convergence threshold 10^{-8} Ry. TlBiSe2 converges in 13 SCF steps (207.6 s). For the 20-material validation (Section 3.4), materials are selected from 811 candidates meeting: DFT-stable, CHGNet-unstable, $\max Z \leq 56$, $n_{\text{sites}} \leq 24$. Structures use golden-ratio fractional coordinate spacing ($\phi = (1 + \sqrt{5})/2$; deterministic, non-overlapping) with DFT-derived cell volumes from WBM. Each SCF calculation runs on 8 CPU cores with a 3,600 s timeout. All 20 converge: 18 on first pass (47 min total) and 2 after retry with expanded cells and tighter mixing (additional 2 hours). Total first-pass wall time for all 20 attempts is 54 min including the 2 that initially failed.

5.8 Cross-MLIP evaluation

Three architecturally distinct MLIPs—CHGNet v0.3.0¹, TensorNet (MatPES-PBE-v2025.1-PES via `matgl` 2.0.6, evaluated in float32 precision), and MACE-MP medium⁴ (via `mace-torch`, float64)—are evaluated on 5,000 WBM materials (random sample, seed = 42). Structures are built from WBM composition, volume, and Wyckoff symmetry data using golden-ratio fractional coordinate spacing with correct DFT-derived cell volumes. Six pairwise correlations (energy and force) are computed with bootstrap 95% CIs (1,000 resamples). Force failure threshold: 50 eV \AA^{-1} .

Data Availability

The WBM benchmark (25,000 materials), all experimental runs and generated Lean 4 proofs are included in the repository. The full WBM dataset (257K) is available from Matbench Discovery².

Code Availability

PCM is open-source at https://github.com/abhinaba/alloy_pcm.

Reproduction: `pip install -e . && python -m pcm demo`.

Acknowledgements

We thank the developers of CHGNet, MACE and TensorNet for making their models publicly available, and the Matbench Discovery team for the WBM benchmark infrastructure.

Author Contributions

A.B. conceived the project, developed the PCM framework, performed all experiments and wrote the manuscript. P.C. supervised the project and reviewed the manuscript.

Competing Interests

The authors declare no competing interests.

References

- [1] Deng, B. et al. CHGNet as a pretrained universal neural network potential for charge-informed atomistic modelling. *Nat. Mach. Intell.* **5**, 1031–1041 (2023).
- [2] Riebesell, J. et al. Matbench Discovery—A framework to evaluate machine learning crystal stability predictions. *Nat. Mach. Intell.* **7**, 836–847 (2025).
- [3] Wang, H.-C., Botti, S. & Marques, M. A. L. Predicting stable crystalline compounds using chemical similarity. *npj Comput. Mater.* **7**, 12 (2021).
- [4] Batatia, I. et al. MACE: Higher order equivariant message passing neural networks for fast and accurate force fields. *NeurIPS* (2022).
- [5] de Moura, L. & Ullrich, S. The Lean 4 theorem prover and programming language. *CADE-28* (2021).

- [6] Cornelio, C. et al. Combining data and theory for derivable scientific discovery with AI-Descartes. *Nat. Commun.* **14**, 1777 (2023).
- [7] Dreossi, T., Donze, A. & Seshia, S. A. Compositional falsification of cyber-physical systems with machine learning components. *J. Autom. Reason.* **63**, 1031–1053 (2019).
- [8] Ernst, D. et al. ARCH-COMP 2023 Category Report: Falsification. *EPiC Ser. Comput.* (2023).
- [9] Walters, J. et al. PhysLean: Digitizing physics with Lean. *arXiv:2405.10000* (2024).
- [10] Dunn, A. et al. Benchmarking materials property prediction methods: the Matbench test suite. *npj Comput. Mater.* **6**, 138 (2020).
- [11] Yoo, S. et al. Learning atomic forces from uncertainty-calibrated adversarial attacks on graph neural network potentials. *npj Comput. Mater.* **11**, 200 (2025).
- [12] Kulichenko, M. et al. Uncertainty-driven dynamics for active learning of interatomic potentials. *Nat. Comput. Sci.* **3**, 230–239 (2023).
- [13] Dalrymple, D. et al. Towards Guaranteed Safe AI: A framework for ensuring robust and reliable AI systems. *arXiv:2405.06624* (2024).
- [14] Deng, B. et al. Systematic softening in universal machine learning interatomic potentials. *npj Comput. Mater.* **11**, 9 (2025).
- [15] Necula, G. C. Proof-carrying code. *POPL* 106–119 (1997).
- [16] Hawkins, R. et al. Guidance on the assurance of machine learning in autonomous systems (AM-LAS). *arXiv:2102.01564* (2021).
- [17] Seshia, S. A., Sadigh, D. & Sastry, S. S. Toward verified artificial intelligence. *Commun. ACM* **65**, 46–55 (2022).
- [18] AlphaProof team. Formal mathematical reasoning with reinforcement learning. *Nature* (2025).
- [19] Angelopoulos, A. N. et al. Conformal risk control. *ICLR* (2024).
- [20] Xu, H. et al. Evidential deep learning for interatomic potentials. *Nat. Commun.* (2025).
- [21] Zhang, H. et al. AlloyGPT: An autoregressive large language model for alloy prediction and design. *npj Comput. Mater.* **11**, 68 (2025).
- [22] Gupta, V. et al. AlloyBERT: Alloy property prediction with large language models. *Comput. Mater. Sci.* **246**, 113433 (2024).
- [23] Xie, T. et al. DARWIN: A series of foundation models for materials science. *arXiv:2412.11970* (2024).
- [24] Rubungo, A. N. et al. LLM-Prop: Predicting physical and electronic properties of crystalline solids from their text descriptions. *npj Comput. Mater.* **11**, 36 (2025).

- [25] Antunes, L. M. et al. Crystal structure generation with autoregressive large language modelling. *Nat. Commun.* **15**, 10570 (2024).
- [26] Sato, T. et al. Direct evidence for the Dirac-cone topological surface states in the ternary chalcogenide TlBiSe₂. *Phys. Rev. Lett.* **105**, 136802 (2010).
- [27] Simeon, G. & de Fabritiis, G. TensorNet: Cartesian tensor representations for efficient and accurate interatomic potentials. *NeurIPS* (2023).
- [28] Chen, C. et al. MatPES: A universal pretrained potential for materials science. *arXiv:2501.11768* (2025).
- [29] Gal, Y. & Ghahramani, Z. Dropout as a Bayesian approximation: Representing model uncertainty in deep learning. *ICML* (2016).
- [30] Lakshminarayanan, B., Pritzel, A. & Blundell, C. Simple and scalable predictive uncertainty estimation using deep ensembles. *NeurIPS* (2017).
- [31] Musil, F. et al. Fast and accurate uncertainty estimation in chemical machine learning. *J. Chem. Theory Comput.* **15**, 906–915 (2019).
- [32] Hirschfeld, L. et al. Uncertainty quantification using neural networks for molecular property prediction. *J. Chem. Inf. Model.* **60**, 3770–3780 (2020).
- [33] Goodfellow, I. J., Shlens, J. & Szegedy, C. Explaining and harnessing adversarial examples. *ICLR* (2015).
- [34] Madry, A. et al. Towards deep learning models resistant to adversarial attacks. *ICLR* (2018).
- [35] Choudhary, K. & DeCost, B. Atomistic line graph neural network for improved materials property predictions. *npj Comput. Mater.* **7**, 185 (2021).
- [36] Park, Y. et al. Scalable parallel algorithm for graph neural network interatomic potentials in molecular dynamics simulations. *J. Chem. Theory Comput.* **20**, 4857–4868 (2024).
- [37] Liao, Y.-L. & Smidt, T. EquiformerV2: Improved equivariant transformer for scaling to higher-degree representations. *ICLR* (2024).
- [38] Merchant, A. et al. Scaling deep learning for materials discovery. *Nature* **624**, 80–85 (2023).
- [39] Choudhary, K. et al. The joint automated repository for various integrated simulations (JARVIS) for data-driven materials design. *npj Comput. Mater.* **6**, 173 (2020).
- [40] Kirklin, S. et al. The Open Quantum Materials Database (OQMD): Assessing the accuracy of DFT formation energies. *npj Comput. Mater.* **1**, 15010 (2015).
- [41] Curtarolo, S. et al. AFLOW: An automatic framework for high-throughput materials discovery. *Comput. Mater. Sci.* **58**, 218–226 (2012).
- [42] Jain, A. et al. Commentary: The Materials Project: A materials genome approach to accelerating materials innovation. *APL Mater.* **1**, 011002 (2013).

- [43] Katz, G. et al. Reluplex: An efficient SMT solver for verifying deep neural networks. *CAV* (2017).
- [44] Huang, X. et al. A survey of safety and trustworthiness of deep neural networks: Verification, testing, adversarial attack and defence, and interpretability. *Comput. Sci. Rev.* **37**, 100270 (2020).
- [45] Amodei, D. et al. Concrete problems in AI safety. *arXiv:1606.06565* (2016).
- [46] Jablonka, K. M. et al. 14 examples of how LLMs can transform materials science and chemistry: A reflection on a large language model hackathon. *Digital Discovery* **3**, 781–810 (2024).
- [47] Miret, S. & Krishnan, N.M.A. Are LLMs ready for real-world materials discovery? *arXiv:2402.05200* (2024).
- [48] White, A. D. et al. Assessment of chemistry knowledge in large language models that generate code. *Digital Discovery* **2**, 368–376 (2023).
- [49] Ramakrishnan, R., Dral, P. O., Rupp, M. & von Lilienfeld, O. A. Quantum chemistry structures and properties of 134 kilo molecules. *Sci. Data* **1**, 140022 (2014).
- [50] Lookman, T. et al. Active learning in materials science with emphasis on adaptive sampling using uncertainties for targeted design. *npj Comput. Mater.* **5**, 21 (2019).
- [51] Smith, J. S. et al. Less is more: Sampling chemical space with active learning. *J. Chem. Phys.* **148**, 241733 (2018).
- [52] Schütt, K. T., Sauceda, H. E., Kindermans, P.-J., Tkatchenko, A. & Müller, K.-R. SchNet – A deep learning architecture for molecules and materials. *J. Chem. Phys.* **148**, 241722 (2018).
- [53] Gasteiger, J., Giri, S., Margraf, J. T. & Günnemann, S. Fast and uncertainty-aware directional message passing for non-equilibrium molecules. In *Machine Learning for Molecules Workshop, NeurIPS* (2020).

Extended Data

Table Extended Data Table 1. Full adversary strategy comparison (10 configurations, budget = 200). CX rate with Wilson 95% CI, failure mode entropy, and unique materials discovered. LLM adversaries achieve higher CX rates but lower unique discovery counts; algorithmic strategies provide broader coverage. Grid and LHS strategies are omitted as they perform comparably to Random and Sobol at this budget.

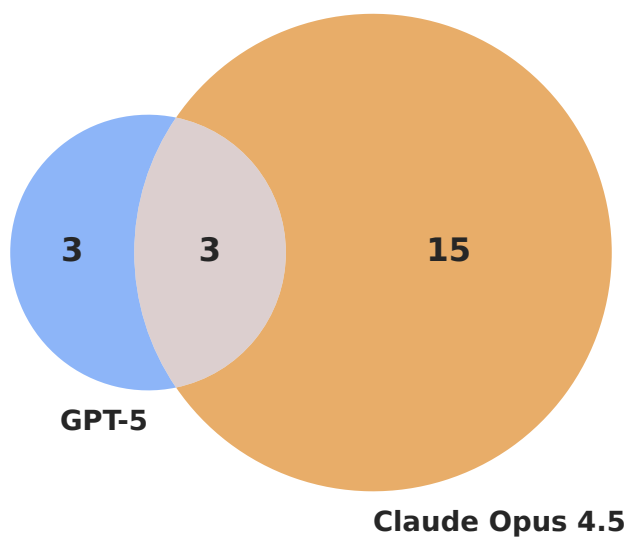
Rank	Strategy	CX Rate	95% CI	Entropy (bits)	Unique
1	Gemini 2.5 Pro (LLM)	100.0%	[98.1, 100]	0.000	5
2	GPT-5 (LLM)	100.0%	[98.1, 100]	0.875	6
3	Gemini 3 Flash (LLM)	98.5%	[95.7, 99.5]	0.980	17
4	GPT-5.2 (LLM)	98.5%	[95.7, 99.5]	0.998	29
5	Claude Opus 4.6 (LLM)	88.5%	[83.3, 92.2]	0.986	20
6	Claude Opus 4.5 (LLM)	88.5%	[83.3, 92.2]	1.211	22
7	Sobol	87.0%	[81.6, 91.0]	1.152	138
8	Random	86.0%	[80.5, 90.1]	1.027	123
9	Heuristic	86.0%	[80.5, 90.1]	0.948	61
10	Claude Sonnet 4.5 (LLM)	86.0%	[80.5, 90.1]	0.729	30

Table Extended Data Table 2. Independent DFT validation of 20 adversarially discovered materials (QE pw.x v6.7, PAW-PBE, SSSP v1.3.0, 60/480 Ry, 8 cores). All 20 converge (2 require expanded cells on retry). DFT E/atom is total energy (including core electrons); CHGNet F_{max} is evaluated on the same golden-ratio structure for direct force comparison. Cu_7Zn_1 (brass) and Cu_7Mn_1 (manganese bronze) are industrial alloys where CHGNet underestimates forces by 15–33 \times .

#	Formula	Atoms	Pred. err. (eV atom ⁻¹)	DFT F_{max} (eV Å ⁻¹)	CHGNet F_{max} (eV Å ⁻¹)	Ratio DFT/CHGNet	SCF	Time (s)
1	Cu_7Zn_1	8	10.49	557	36	15.4 \times	15	180
2	Cd_6Zr_2	8	10.09	460	28	16.5 \times	14	153
3	$\text{Ag}_6\text{Cl}_2\text{S}_2$	10	9.98	1445	39	36.8 \times	13	296
4	RuZn_3	4	9.95	89	54	1.6 \times	11	22
5	LiO_4Sc_3	8	9.74	197	22	8.8 \times	18	71
6	Cu_6Mg_2	8	9.68	321	24	13.2 \times	14	60
7	Cu_6Ga_3	9	9.54	2154	194	11.1 \times	20	178
8	F_6SnSr	8	9.41	298	61	4.9 \times	12	43
9	Y_2Zn_6	8	9.39	342	15	22.5 \times	13	172
10	$\text{Ba}_2\text{Pd}_4\text{Sb}_4$	10	9.38		<i>Retry</i> [†]		37	6360
11	BaF_6In	8	9.34		<i>Retry</i> [†]		150	1345
12	In_6Sb_2	8	9.27	287	9	31.3 \times	12	214
13	$\text{Cu}_2\text{O}_2\text{Te}_2\text{Y}_2$	8	9.25	322	40	8.0 \times	14	88
14	Cu_7Mn_1	8	9.24	530	16	33.1 \times	17	95
15	$\text{Cd}_4\text{Ni}_2\text{Sr}_2$	8	9.13	351	29	12.3 \times	15	194
16	$\text{Ca}_2\text{In}_2\text{Zn}_4$	8	9.10	334	36	9.4 \times	13	256
17	Zn_3Zr	4	9.10	61	43	1.4 \times	11	24
18	$\text{As}_2\text{In}_4\text{Pd}_6$	12	9.05	2222	35	63.4 \times	17	537
19	$\text{Ag}_2\text{Ba}_2\text{O}_4$	8	9.04	230	66	3.5 \times	36	191
20	$\text{F}_6\text{K}_2\text{Mg}$	9	8.99	97	80	1.2 \times	14	52

[†]Converged on retry with expanded cells (5 \times and 4 \times volume) and tighter mixing ($\beta = 0.1$, 80/640 Ry). Force comparison omitted as structures differ from original golden-ratio placement.

Figure 5: Dual-Adversary Discovery Coverage



Union: 21 unique materials | Overlap: 14.3%

GPT-5: focused depth (6 total) | Opus 4.5: broad coverage (18 total)

Figure Extended Data Fig. 1. Dual-adversary Venn diagram. Two adversary strategies discover complementary materials with 14.3% overlap (3 consensus materials). Complementary search strategies exploit different regions of compositional space.

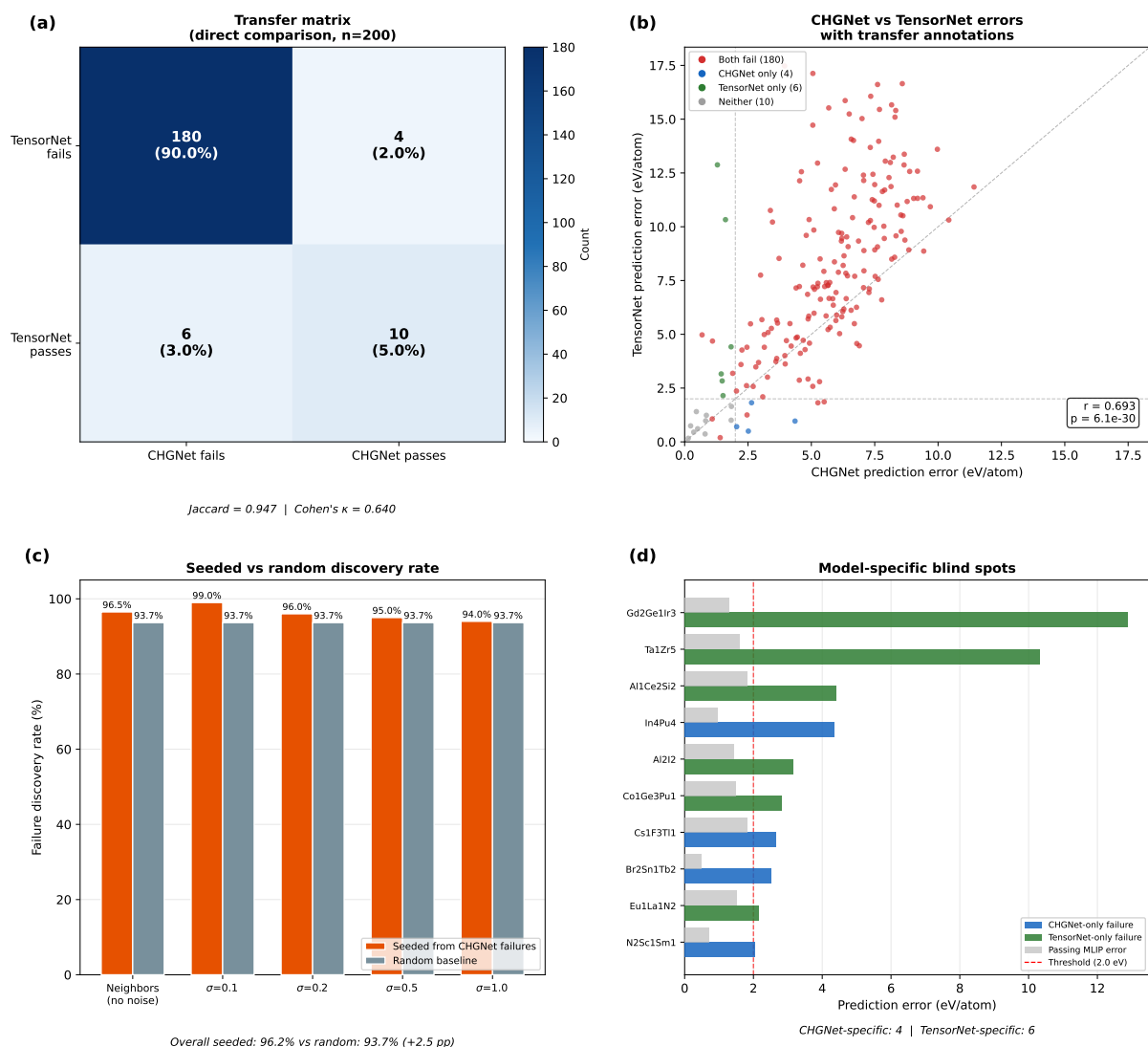


Figure Extended Data Fig. 2. Cross-MLIP adversarial transfer. **a**, CHGNet \leftrightarrow TensorNet transfer rate heatmap: 97.8% of CHGNet failures also fail on TensorNet. **b**, Error correlation scatter ($r = 0.69$). **c**, Seeded vs random discovery rates. **d**, Model-specific blind spots.

JARVIS-DFT (OptB88vdW) Cross-Oracle Comparison
n=814 matched materials, CHGNet-JARVIS agreement=15.2%

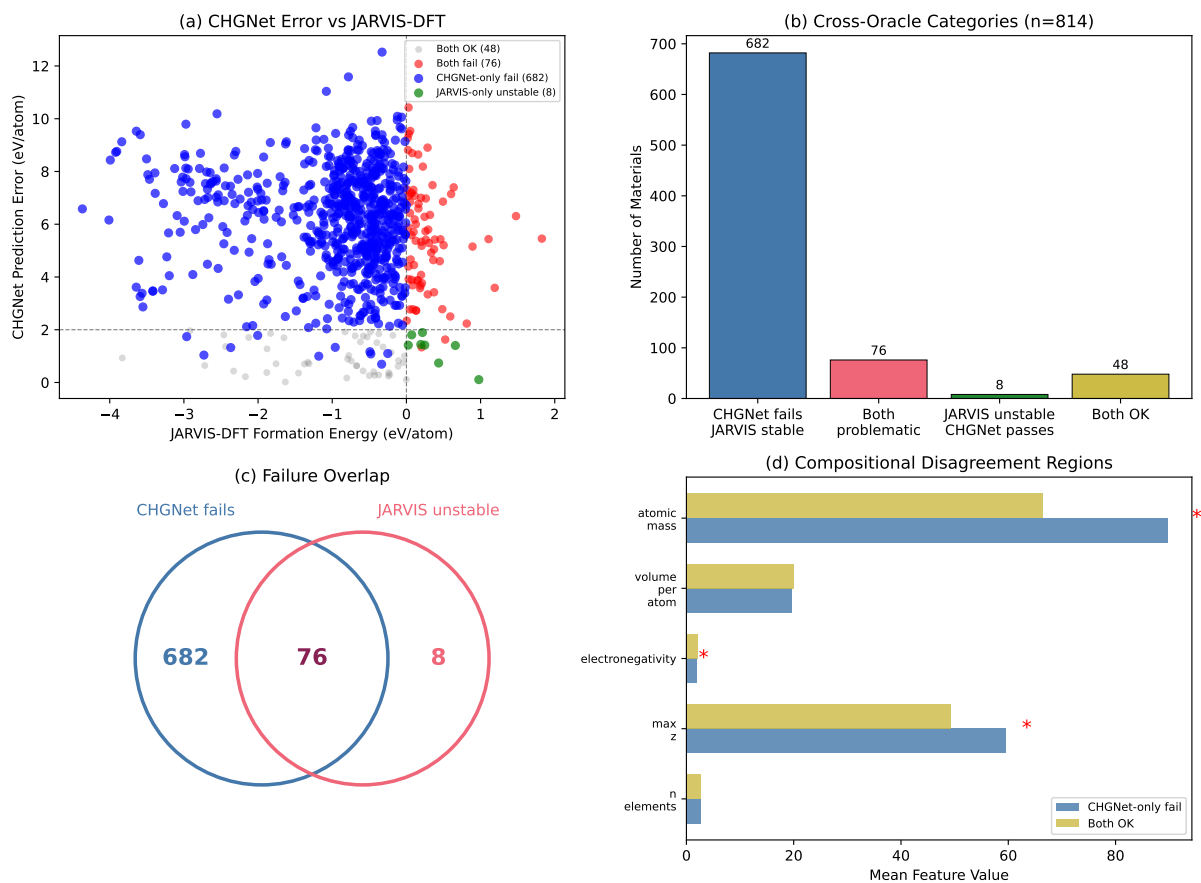


Figure Extended Data Fig. 3. JARVIS-DFT cross-oracle validation. **a**, CHGNet prediction error vs JARVIS formation energy for 814 matched materials. **b**, Cross-oracle category counts: 682 CHGNet-only failures. **c**, Failure overlap Venn diagram. **d**, Compositional features of disagreement regions: max Z ($p = 0.002$) and mean atomic mass ($p = 7 \times 10^{-5}$) significantly higher in CHGNet blind spots.

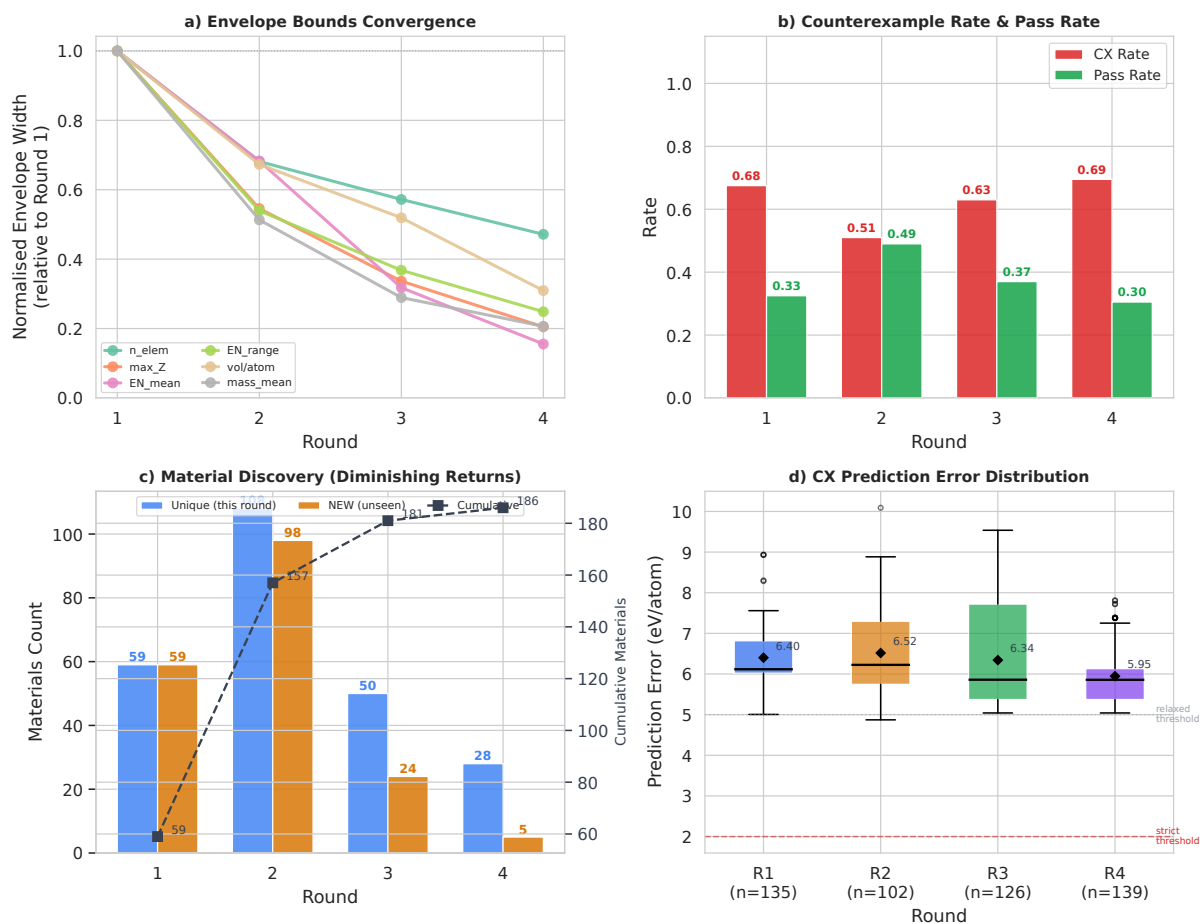


Figure Extended Data Fig. 4. Iterative envelope refinement (4 rounds). **a**, Envelope bounds convergence. **b**, CX/pass rate evolution. **c**, Cumulative material discovery. **d**, Error distribution per round. The safe envelope compresses by 75–91% per feature dimension.

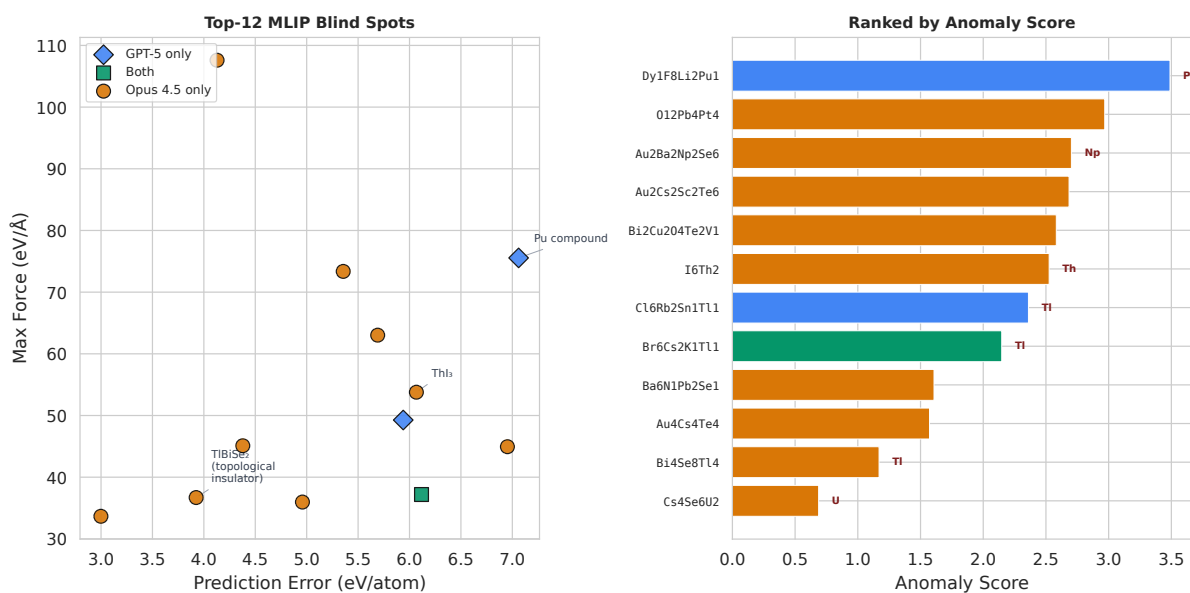


Figure Extended Data Fig. 5. Element frequency analysis. **a**, Per-element mean prediction error vs WBM frequency (84 elements, Spearman $\rho = 0.443$). **b**, Stability disagreement by periodic table block: f-block highest (Kruskal–Wallis $p = 0.042$). **c**, Adversarial vs non-adversarial elements ($p = 0.020$). Rarest quintile contains 41% adversarial elements.

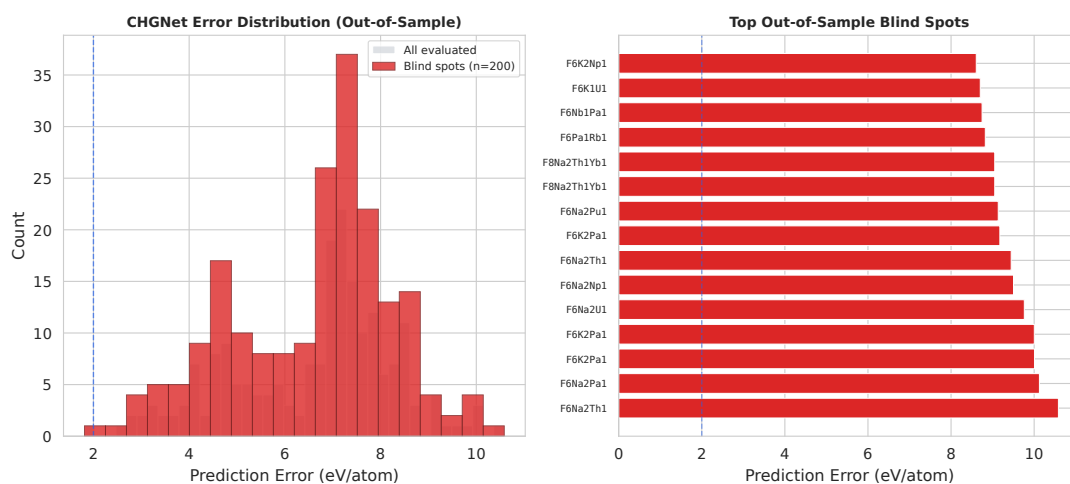
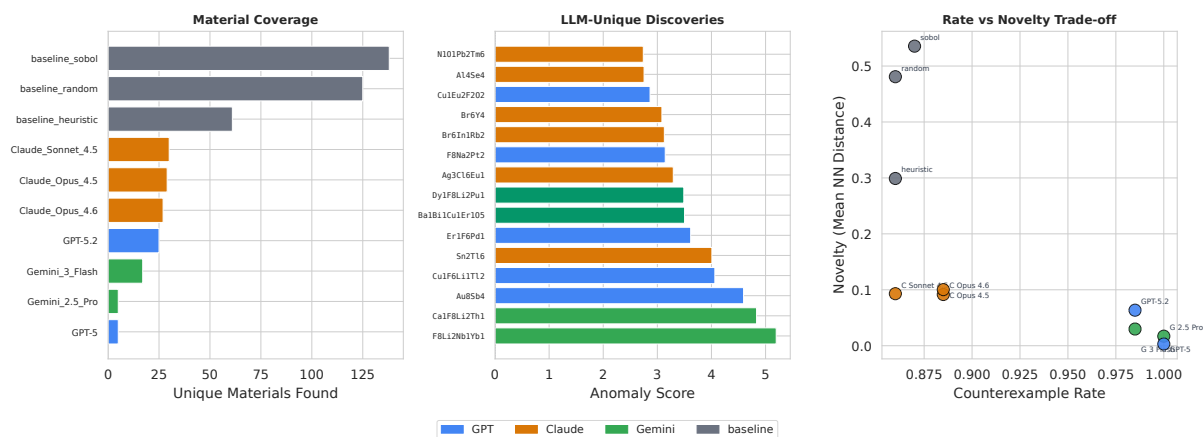


Figure Extended Data Fig. 6. Adversarial strategy analysis. **Top:** Ablation comparing 13 adversary configurations on CX rate vs unique materials discovered (base CX rate = 93.2%; max-everything achieves 100% but discovers only 1 unique material). **Bottom:** Emergent search behaviour—**a**, Feature-space autocorrelation. **b**, Phase transition detection. **c**, Post-violation exploration ($p = 0.0001$).

Shuffled-Feature Ablation: Does the LLM Use Domain Knowledge?

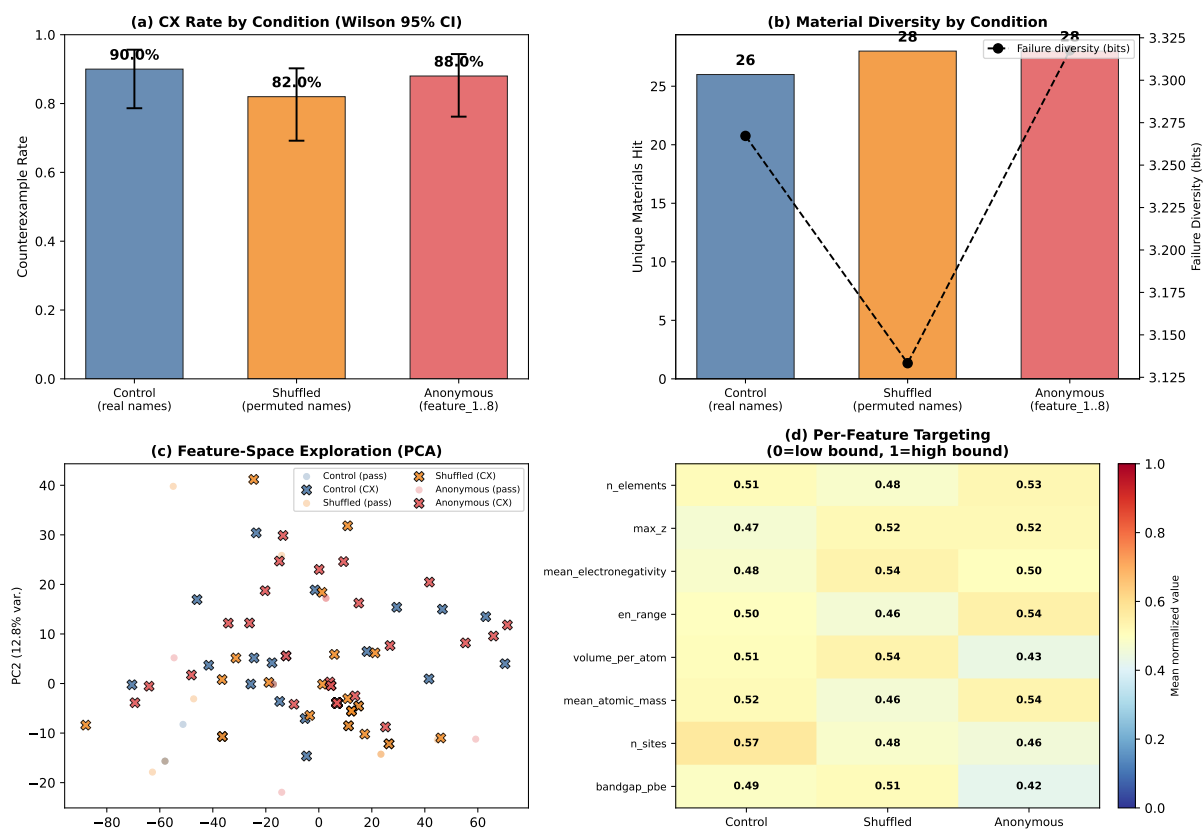


Figure Extended Data Fig. 7. Shuffled-feature ablation. CX rate by condition: control 90%, shuffled 82%, anonymous 88% (Wilson 95% CIs). Incorrect domain knowledge (shuffled) is worse than no knowledge (anonymous), confirming the adversary-oracle separation as the core mechanism.

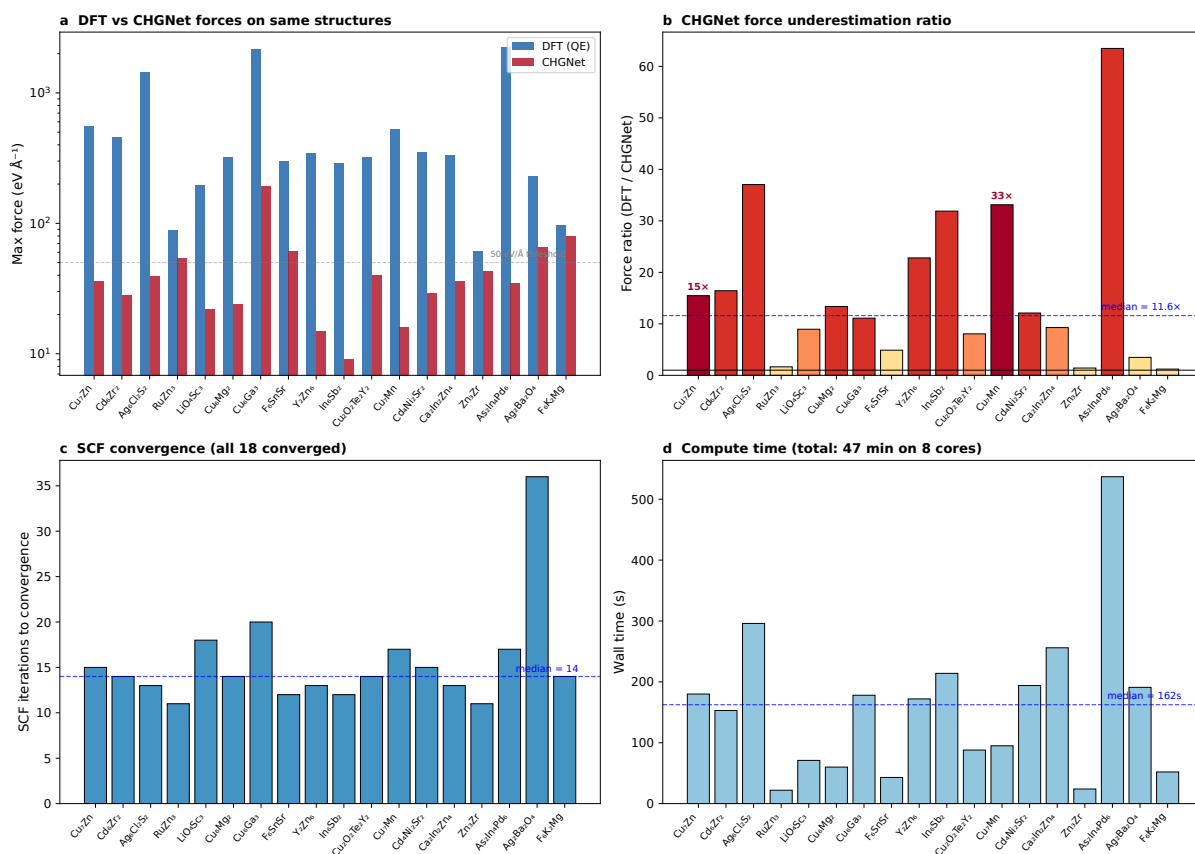


Figure Extended Data Fig. 8. Independent DFT validation of adversarially discovered MLIP blind spots (18 materials with identical golden-ratio structures; 2 retry materials excluded from force comparison). **a**, Maximum forces from Quantum ESPRESSO (DFT) vs CHGNet on the same structures (log scale). DFT forces are systematically larger, confirming CHGNet underestimates instability. **b**, Force ratio (DFT/CHGNet); median 11.6 \times . Cu₇Zn₁ (brass, 15 \times) and Cu₇Mn₁ (manganese bronze, 33 \times) are highlighted. **c**, SCF iterations to convergence (median 14). **d**, Wall-clock time per material (total 47 min on 8 CPU cores).

Figure Extended Data Fig. 9. Representative Lean4 proof output for the WBM–CHGNet safety certificate (auto-generated from the refined envelope). **Top:** The core safety module defines compositional bounds (`EnvBounds`), structural requirements (`DesignReq`), and outcome thresholds (`HoldsThresholds`). The `oracle_guarantee` axiom—the only unverified assumption—states that the MLIP satisfies thresholds within the envelope; a domain expert can inspect whether this assumption is warranted. `safe_under_envelope` composes these into the safety claim; `envelope_non_vacuous` provides a constructive witness proving the envelope is non-empty. **Bottom:** The error propagation module composes DFT accuracy ($\epsilon_{\text{DFT}} = 0.1 \text{ eV atom}^{-1}$) with the MLIP threshold via the triangle inequality, making the full approximation chain (reality \rightarrow DFT \rightarrow MLIP) explicit and auditable. All proofs are verified by `lake build` (Lean 4.27.0).

Generated.lean — Core safety certificate (WBM–CHGNet)

```

1  structure Env where
2    n_elements : Real; max_z : Real
3    mean_electronegativity : Real; en_range : Real
4    volume_per_atom : Real; mean_atomic_mass : Real
5
6  structure Design where
7    n_sites : Real; bandgap_pbe : Real
8
9  structure Outcomes where
10   prediction_error : Real; max_force : Real
11
12  -- Bounds from the adversarially refined envelope
13  def EnvBounds (e : Env) : Prop :=
14    (1 <= e.n_elements && e.n_elements <= 4.41)
15    && (3 <= e.max_z && e.max_z <= 62.21)
16    && (0.7 <= e.mean_electronegativity && e.mean_electronegativity <= 3.17)
17    && (5 <= e.volume_per_atom && e.volume_per_atom <= 48.90)
18    && (5 <= e.mean_atomic_mass && e.mean_atomic_mass <= 159.65)
19
20  def HoldsThresholds (o : Outcomes) : Prop :=
21    (o.prediction_error <= 2) && (o.max_force <= 50)
22
23  -- Key assumption (the only axiom a reviewer must evaluate):
24  axiom oracle_guarantee :
25    forall e d, EnvBounds e -> DesignReq d -> HoldsThresholds (oracle e d)
26
27  -- Safety: if env and design are within the envelope, thresholds hold.
28  theorem safe_under_envelope :
29    forall e d, EnvBounds e -> DesignReq d -> SafeClaim e d := by
30      intro e d hE hD
31      exact And.intro hE (And.intro hD (oracle_guarantee e d hE hD))
32
33  -- Non-vacuity: a concrete witness proves the envelope is non-empty.
34  theorem envelope_non_vacuous :
35    exists e d, EnvBounds e && DesignReq d := by
36      refine <2.71, 32.60, 1.93, 1.12, 26.95, 82.32>, <17.40, 2.92>, ...
37      all_goals norm_num

```

ErrorPropagation.lean — Composing DFT + MLIP uncertainty

```

1  -- Triangle inequality: |E_true - E_MLIP| <= |E_true - E_DFT| + |E_DFT - E_MLIP|
2  theorem total_uncertainty_bound
3    (c : EnergyChain) (eps_mlip : Real)
4    (h_dft : DFTAccurate c pbe_accuracy) -- pbe_accuracy = 0.1 eV/atom
5    (h_mlip : MLIPAccurate c eps_mlip) :
6    TotalAccurate c (pbe_accuracy + eps_mlip) := by
7      exact interval_composition c pbe_accuracy eps_mlip h_dft h_mlip
8
9  -- Full safety with explicit uncertainty budget:
10  -- Within the envelope, MLIP agrees with physical reality
11  -- within 0.1 + claim_threshold = 0.6 eV/atom.
12  -- Every approximation layer is transparent and auditable.

```